nature cell biology

Endolysosomal sorting of ubiquitylated caveolin-1 is regulated by VCP and UBXD1 and impaired by VCP disease mutations

Danilo Ritz[1,2,7], Maja Vuk[1,2,7], Philipp Kirchner[1], Monika Bug[1], Sabina Schütz[2], Arnold Hayer[2], Sebastian Bremer[1], Caleb Lusk[3], Robert H. Baloh[3], Houkeun Lee[4], Timo Glatter[4,5], Matthias Gstaiger[4,5], Ruedi Aebersold[4,5,6], Conrad C. Weihl[3,8] and Hemmo Meyer[1,2,8]

The AAA-ATPase VCP (also known as p97) cooperates with distinct cofactors to process ubiquitylated proteins in different cellular pathways[1–3]. VCP missense mutations cause a systemic degenerative disease in humans, but the molecular pathogenesis is unclear[4,5]. We used an unbiased mass spectrometry approach and identified a VCP complex with the UBXD1 cofactor, which binds to the plasma membrane protein caveolin-1 (CAV1) and whose formation is specifically disrupted by disease-associated mutations. We show that VCP–UBXD1 targets mono-ubiquitylated CAV1 in SDS-resistant high-molecular-weight complexes on endosomes, which are en route to degradation in endolysosomes[6]. Expression of VCP mutant proteins, chemical inhibition of VCP, or siRNA-mediated depletion of UBXD1 leads to a block of CAV1 transport at the limiting membrane of enlarged endosomes in cultured cells. In patient muscle, muscle-specific caveolin-3 accumulates in sarcoplasmic pools and specifically delocalizes from the sarcolemma. These results extend the cellular functions of VCP to mediating sorting of ubiquitylated cargo in the endocytic pathway and indicate that impaired trafficking of caveolin may contribute to pathogenesis in individuals with VCP mutations.

Valosin-containing protein (VCP) is a hexameric AAA (ATPases associated with diverse cellular activities)-type ATPase best known for targeting and segregating ubiquitin-conjugated protein complexes for subsequent degradation by the proteasome in as diverse cellular processes as endoplasmic reticulum-associated degradation or cell cycle signalling[1–3,7]. VCP cooperates with alternative sets of cofactors, including a group of ubiquitin-like (UBX)-domain-containing proteins, which provide functional and spatial specificity[8,9]. As there are many uncharacterized cofactors, VCP is thought to have many yet unidentified cellular functions[9,10]. VCP missense mutations in humans cause a dominant late-onset systemic degenerative disorder, IBMPFD (inclusion body myopathy associated with Paget's disease of bone and fronto-temporal dementia), also called VCP disease[4,5]. Although cellular defects associated with IBMPFD mutations have been proposed[11–15], the molecular pathogenesis has remained unclear because VCP is essential and patients develop normally until their fourth or fifth decade. As mutant VCP still binds to the main cofactors p47 (also known as NSFL1C) or UFD1–NPL4 (also known as UFD1L–NPLOC4, ubiquitin fusion degradation 1 like–nuclear protein localization 4 homologue) and its ATP hydrolysis activity is only mildly affected at most[15,16], we reasoned that an as yet unidentified function may be specifically affected by the mutations in VCP.

To identify such a function, we used an unbiased mass spectrometry approach (Fig. 1a) to search for a distinct VCP cofactor or substrate, whose interaction may specifically be compromised by the most common disease-associated mutation, R155H (RH; ref. 4). We induced mild overexpression of Myc/Strep-tagged VCP^{RH} in stable HEK293 cells. For comparison, we expressed wild-type VCP or the ATPase-deficient substrate-trapping mutant E578Q (EQ; refs 17,18). Tandem isolation revealed that tagged VCP integrated with endogenous VCP hexamers in a roughly 1:1 ratio (Fig. 1b). We analysed associated proteins using liquid chromatography–tandem mass spectrometry (LC–MS/MS) and compared interaction partners identified with a high probability of $\geq$99% (ref. 19; Fig. 1a and Supplementary Table S1). Eight common cofactors including components of the endoplasmic reticulum-associated degradation system were consistently identified in all samples independent of the VCP variant, implying that the main processes are not affected by the disease-associated VCP^{RH}

[1]Centre for Medical Biotechnology, University of Duisburg-Essen, 45117 Essen, Germany. [2]Institute of Biochemistry, ETH Zurich, 8093 Zurich, Switzerland. [3]Department of Neurology, Washington University School of Medicine, Saint Louis, Missouri 63110, USA. [4]Institute of Molecular Systems Biology, ETH Zurich, 8093 Zurich, Switzerland. [5]Competence Center for Systems Physiology and Metabolic Diseases, ETH Zurich, 8093 Zurich, Switzerland. [6]Faculty of Science, University of Zurich, 8006 Zurich, Switzerland. [7]These authors contributed equally to this work.
[8]Correspondence should be addressed to C.C.W. or H.M. (e-mail: weihlc@neuro.wustl.edu or hemmo.meyer@uni-due.de)

Received 25 March 2011; accepted 21 June 2011; published online 7 August 2011; DOI: 10.1038/ncb2301

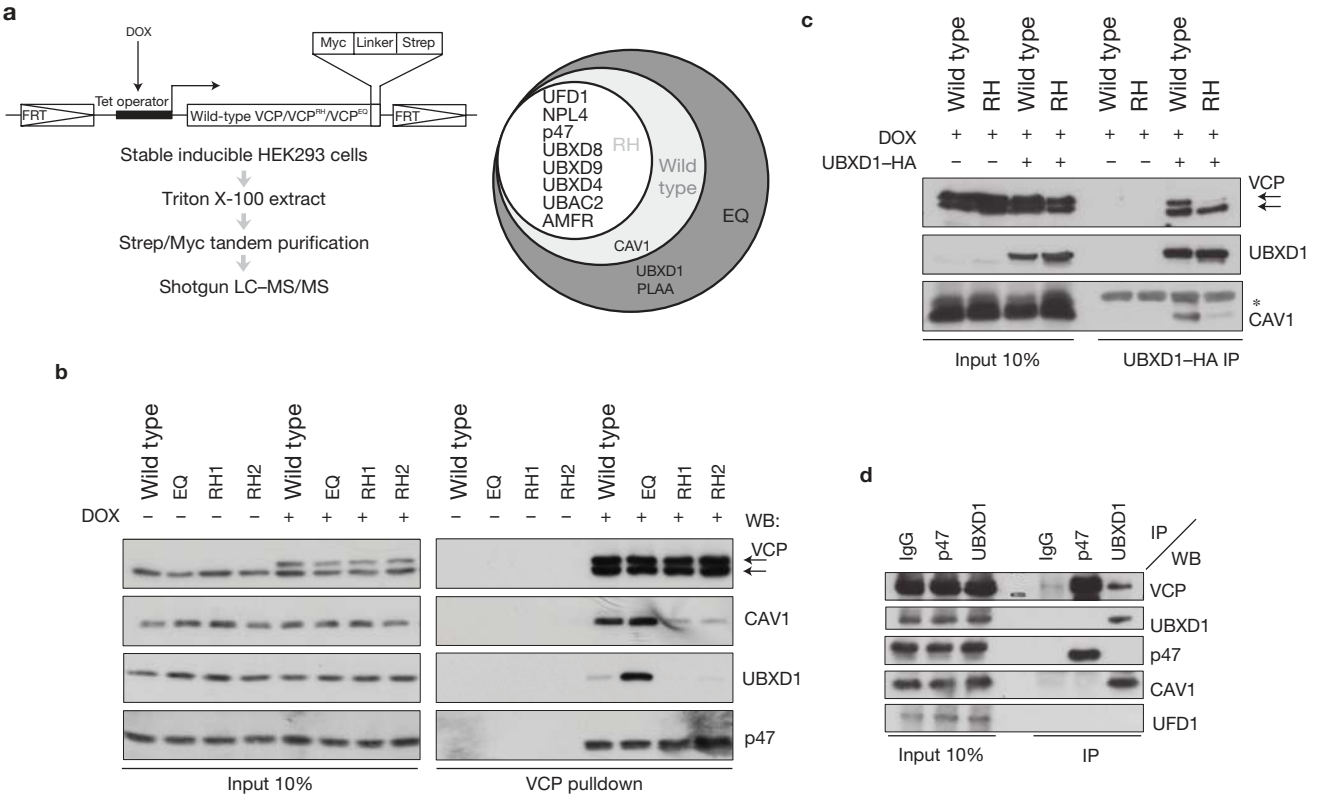

Figure 1 The VCP–UBXD1 chaperone complex binds to caveolin, and this interaction is specifically disrupted by IBMPFD-associated mutations in VCP. (**a**) Mass spectrometry-based strategy to identify differences in the interaction pattern of wild-type VCP, the disease-associated mutant RH or the ATPase-deficient mutant EQ. Left, Myc/Strep-tagged VCP variants were doxycycline (DOX)-induced and tandem isolated from stable HEK293 cell lines. Right, associated proteins were detected in a shotgun approach and high-probability (≥99%) candidates are represented in a Venn diagram. For full details, see Supplementary Table S1. FRT, flippase recognition target. (**b**) Western blot (WB) confirming differential interaction of CAV1 and UBXD1 with overexpressed VCP variants. The p47 cofactor served as a control. RH1 and RH2 represent two independent cell lines. The arrows indicate endogenous and overexpressed VCP. Consistent results for the R95G and A232E disease mutants are shown in Supplementary Fig. S1c. (**c**) Immunoprecipitation (IP) of HA-tagged UBXD1 from cells expressing wild-type VCP or VCP^{RH}. Note the decreased level of binding of VCP^{RH} (upper arrow) and CAV1 in the VCP^{RH} background. The asterisk indicates the position of the antibody light chain. (**d**) Immunoprecipitations of indicated endogenous VCP cofactors with specific antibodies. Note that UBXD1 specifically binds to VCP and CAV1, and is devoid of the p47 or UFD1 cofactors. Uncropped images of blots are shown in Supplementary Fig. S6.

mutation in the HEK293 cells, and consistent with a previous report[11]. This was supported by analysis with the X-box binding protein 1 $(XBP1)^{\Delta DBD}$–Venus reporter assay[20] showing that the endoplasmic reticulum unfolded protein response was not induced by VCP^{RH} overexpression, in contrast to VCP^{EQ} (Supplementary Fig. S1a).

Importantly however, we identified a new VCP binding factor CAV1 as a high-probability hit both in wild-type and EQ, but not in RH isolates (Fig. 1a). Western blot analysis confirmed that CAV1 bound to VCP and that this interaction was specifically compromised by the RH mutation (Fig. 1b). In addition, we detected the UBX domain protein 1 (UBXD1; also known as UBXN6) cofactor[9,21] in EQ isolates (Fig. 1a,b), and found that it also co-isolated with wild-type VCP at lower levels, but not with the RH mutant (Fig. 1b). Binding of UBXD1 and CAV1 to two other IBMPFD-associated VCP mutants, R95G and A232E (AE), was also affected (Supplementary Fig. S1c), implying that compromised binding of VCP to UBXD1 and CAV1 is a general defect underlying the disease. In all cases, the interaction of the VCP mutant proteins with the main cofactors p47 and UFD1–NPL4 was slightly increased (Fig. 1b and Supplementary Fig. S1c), as recently reported[15].

Next, we investigated whether VCP, UBXD1 and CAV1 form a single complex. Sequential isolation of VCP by virtue of its Strep-tag from cells overexpressing all three factors, followed by native elution and immunoprecipitation of UBXD1 co-isolated CAV1, indicating that they form a ternary complex (Supplementary Fig. S1d). Direct isolation of overexpressed UBXD1 from cells expressing wild-type VCP and VCP^{RH} further supported this notion and confirmed that the level of CAV1 binding to UBXD1 was decreased in the RH background (Fig. 1c). Immunoprecipitation of endogenous UBXD1 or p47 with specific antibodies showed that the interaction with CAV1 was specific for the VCP–UBXD1 complex, which did not contain any of the other main cofactors, p47 or UFD1–NPL4 (Fig. 1d). These results demonstrate that UBXD1 defines an alternative VCP complex, which binds to CAV1 and whose formation is specifically compromised by disease-associated mutation of VCP.

CAV1, and its isoforms caveolin-2 and the muscle-specific caveolin-3 (CAV3), are membrane proteins that form the main constituent of caveolae[22]. Caveolae are invaginations of the plasma membrane that define cholesterol-rich microdomains, which are important for signalling, endocytosis and maintenance of the plasma membrane[22]. CAV1 is synthesized in the endoplasmic reticulum and assembles along the membranes of the secretory pathway into large caveolar domains[23–25] that subsequently travel between the

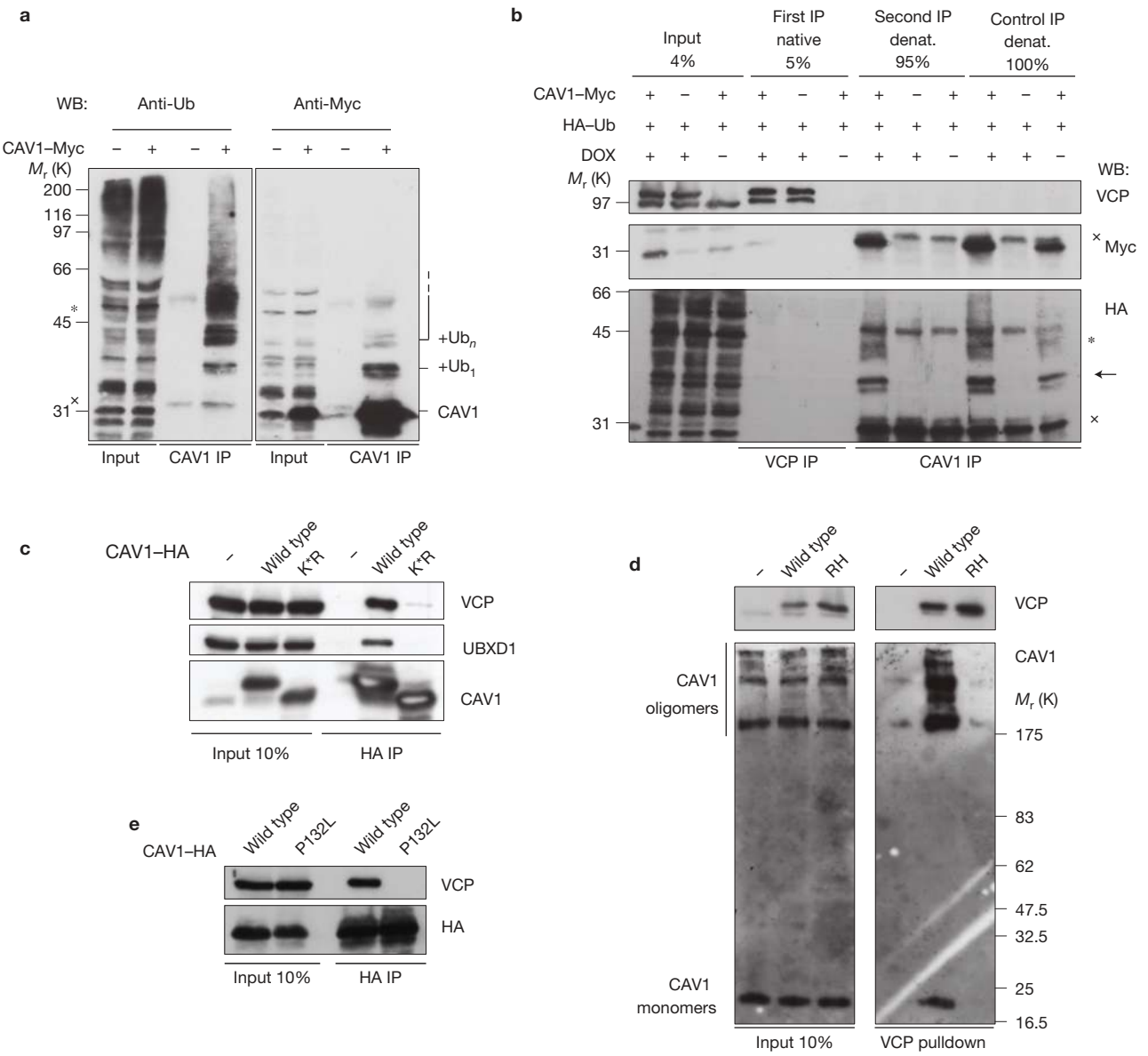

Figure 2 VCP targets mono-ubiquitylated CAV1 in SDS-resistant oligomers. (**a**) Ubiquitin modification of CAV1 was detected with the anti-ubiquitin FK2 or the anti-Myc antibodies after CAV1–Myc expression and isolation with the CAV1-specific N20 antibody. Note the prominent mono-ubiquitylation (Ub_1) and minor multi- and/or polyubiquitylation (Ub_n). (**b**) Sequential immunoprecipitations show that VCP binds to mono-ubiquitylated CAV1 (arrow). First, doxycycline (DOX)-induced VCP was isolated from cells expressing HA–ubiquitin and CAV1–Myc. Then, 5% of it was loaded (first IP), the remaining 95% was denatured to remove associated proteins and CAV1 was re-isolated with the specific N20 antibody (second IP). Direct immunoprecipitation from denatured lysates served as a reference. The asterisk and the cross indicate the positions of the antibody heavy and light chains, respectively. (**c**) Wild-type CAV1–HA or the K*R mutant, whose ubiquitylation is abolished owing to mutation of all 12 lysine residues to arginine, was expressed, and association with VCP and UBXD1 was analysed by CAV1–HA immunoprecipitation. (**d**) VCP preferentially targets SDS-resistant CAV1 oligomers. Wild-type VCP and VCP^{RH} complexes were isolated from CV-1 cells and separated in SDS gels for western blotting (WB) without prior boiling. CAV1 monomers and SDS-resistant oligomers were detected in inputs. Note the specific enrichment of oligomers in VCP complexes. (**e**) The disease-associated and oligomerization-deficient CAV1^{P132L} mutant was overexpressed with HA-tag and immunoprecipitated. Note the decreased level of VCP binding. Uncropped images of blots are shown in Supplementary Fig. S6.

plasma membrane and endosomes[26,27]. For degradation, CAV1 is modified with mono-ubiquitin, a signal important for endosomal sorting[28], and transported to intraluminal vesicles in endolysosomes[6]. In other cellular processes, VCP targets ubiquitin-modified substrate proteins[1–3]. We therefore initially confirmed that CAV1 is conjugated predominantly with mono-ubiquitin in HEK293 cells (Fig. 2a). We then showed in sequential immunoprecipitations that CAV1 associated with VCP in the ubiquitylated form in addition to the unmodified form (Fig. 2b). To determine whether ubiquitylation is essential for the interaction with VCP, we analysed a CAV1^{K*R} variant, in which all 12 lysines were mutated to arginine. CAV1^{K*R} still travels to early endosomes, but cannot be ubiquitylated and transported to endolysosomes[6] (Supplementary Fig. S2). Indeed, co-immunoprecipitations revealed that binding to VCP was abolished (Fig. 2c), implying that CAV1 ubiquitylation is important for targeting by VCP.

During maturation, CAV1 first forms SDS-resistant oligomers that associate to form larger assemblies in a cholesterol-dependent manner during exit from the Golgi apparatus[23,24,29,30]. Similarly to other AAA-type ATPases, VCP uses the energy of ATP hydrolysis to segregate proteins from stable complexes for further processing[17,18,31]. We therefore investigated whether VCP targets SDS-resistant CAV1 oligomers. Lysates of CV-1 control cells, and of CV-1 cells expressing wild-type VCP or VCP^{RH}, were separated on SDS gels without prior boiling and exhibited a typical pattern of SDS-resistant CAV1 complexes above the apparent relative molecular mass of 200,000 (M_r 200K) in western blots[29] (Fig. 2d). Isolation of VCP revealed that the associated CAV1 was enriched in such complexes when compared with the monomeric form in the case of wild-type cells, showing that indeed VCP targets CAV1 oligomers. As expected, VCP^{RH} did not bind to either of the two forms.

To confirm the observed selectivity of VCP for these oligomers, we used two methods to disrupt oligomerization. First, we expressed a CAV1 variant with the P132L mutation that is defective in oligomerization[32]. Second, we depleted plasma membrane pools of cholesterol with the inhibitor U18666A (ref. 23). In both cases, the level of VCP binding in pulldown experiments was decreased or abolished (Fig. 2e and Supplementary Fig. S1e). The large assemblies separate from the individual SDS-resistant complexes in velocity centrifugation gradients with sedimentation coefficients of 70S and 8S, respectively[23]. Both peaks sedimented normally in lysates from cells expressing wild-type VCP or VCP^{RH}, whereas the 70S selectively shifted to the bottom of the gradient in VCP^{EQ} lysates (Supplementary Fig. S1f). Together, these data provide biochemical evidence implying that the VCP–UBXD1 complex binds to the caveolin oligomers that occur post-Golgi at or near the plasma membrane.

To confirm this notion morphologically, we assessed co-localization of CAV1–GFP (green fluorescent protein) with UBXD1–mCherry overexpressed in live U2OS cells. CAV1 localized to caveolae at the plasma membrane in addition to larger intracellular structures (Fig. 3a). UBXD1 specifically co-localized with CAV1 to these structures, in addition to its diffuse cytosolic distribution (Fig. 3a). The intracellular structures were the previously described endocytic compartments[6], because they co-localized with GFP fusions of markers for early and late endosomes, RAB5 (also known as RAB5A, member RAS oncogene family), RAB7 (also known as RAB7A) and LAMP1 (lysosomal-associated membrane protein 1; Supplementary Fig. S2a,b). Consistent with the biochemical analysis, recruitment of UBXD1 to endosomes required ubiquitylation of CAV1, because UBXD1 did not associate with endosomes in cells transfected with the $CAV1^{K*R}$ variant that failed to be ubiquitylated (Supplementary Fig. S2c–f).

Next, we investigated whether VCP and UBXD1 were essential for trafficking of CAV1 to endolysosomes and whether disease-associated mutants were defective in the process. In the first approach, we induced expression of VCP mutants in stable U2OS cells transiently expressing CAV1–RFP (red fluorescent protein) along with LAMP1–GFP as a marker for late endosomes and lysosomes. CAV1 co-localized with LAMP1 in control cells (Fig. 3b), confirming that part of it was transported to endolysosomes[6]. Strikingly however, CAV1 in VCP^{RH}- and more so in VCP^{EQ}-expressing cells localized to enlarged LAMP1-positive vesicles that appeared as early as 24 h after induction of mutant VCP (Fig. 3b,c). Importantly, CAV1 was restricted to the limiting membrane of these vesicles, which points to a defect in processing and transport of CAV1 to intraluminal vesicles. Ultrastructural analysis revealed that the number of multivesicular bodies (MVBs) was indeed decreased in cells expressing VCP^{EQ}, VCP^{RH} or another disease-associated mutant, VCP^{AE} (Fig. 3d,e and Supplementary Fig. S3a). Instead, we observed an increased number of vacuoles that were empty or contained only few intraluminal vesicles. Further fluorescence microscopy analysis using the pH-sensitive lysotracker probe revealed that the aberrant CAV1/LAMP1-rimmed vesicles failed to acidify (Supplementary Fig. S3b). They were not autophagosomes, because they did not contain the autophagy marker LC3 (also known as MAP1LC3A, microtubule-associated protein 1 light chain 3α; Supplementary Fig. S3c). Cellular depletion of UBXD1 by short interfering RNA (siRNA) also specifically affected transport of CAV1, as shown by an increase in the number of enlarged CAV1/RAB5-positive endosomes (Fig. 3f–h). These data show that binding and activity of VCP and its cofactor UBXD1 are required for proper sorting of CAV1 to endolysosomes.

In an additional approach, we applied the VCP small-molecule inhibitor DBeQ (ref. 33). Treatment for 6 h induced accumulation of overexpressed CAV1–GFP at enlarged LAMP1-rimmed vesicles, exceeding the effect of VCP^{EQ} expression markedly (Fig. 4a). Even without overexpression of CAV1, DBeQ caused an enlargement of LAMP1-positive late endosomes/lysosomes and an accumulation of CAV1 in more than 80% of these structures (Fig. 4b), implying that acute and penetrant inhibition of VCP affects trafficking also of endogenous CAV1. Next, we investigated whether inhibition of VCP had a more general impact on the cargo of the endocytic pathway and assessed degradation of the epidermal growth factor receptor (EGFR). After epidermal growth factor (EGF) stimulation, the EGFR was endocytosed normally in control and DBeQ-treated cells, as visualized by immunohistochemistry, but then persisted longer in intracellular pools in DBeQ-treated cells when compared with control-treated cells (Fig. 4c). The delayed degradation of the EGFR was also confirmed by western blot analysis (Fig. 4d). Chemical inhibition thus confirmed the role of VCP in CAV1 trafficking and revealed a more general involvement in endosomal sorting.

To assess whether the role of VCP in caveolin trafficking is relevant to IBMPFD patients, we first analysed cultured fibroblasts from three different patients harbouring two different VCP mutations (see Supplementary Table S2 for patient demographics). We compared the distribution of endogenous CAV1 and LAMP2 by immunofluorescence microscopy with cells from healthy individuals or patients with another degenerative disorder, sporadic amyotrophic lateral sclerosis (sALS). Again, CAV1 accumulated on the limiting membrane of enlarged vesicles that were positive for LAMP2 in IBMPFD patient cells when compared with control cells (Fig. 5a,b). Consistently, the vesicles were not acidified and did not contain LC3 (data not shown). Next, we analysed CAV3 localization in muscle tissue from six different IBMPFD patients. Whereas CAV3 in healthy individuals exhibited the typical sarcolemmal localization, it accumulated in sacroplasmic pools that associated and partially overlapped with late endosomes in patient tissue (Fig. 5c and Supplementary Fig. S4a). Strikingly, CAV3 also specifically delocalized from the sacrolemma. This entailed delocalization of its partner protein cavin-1 (also

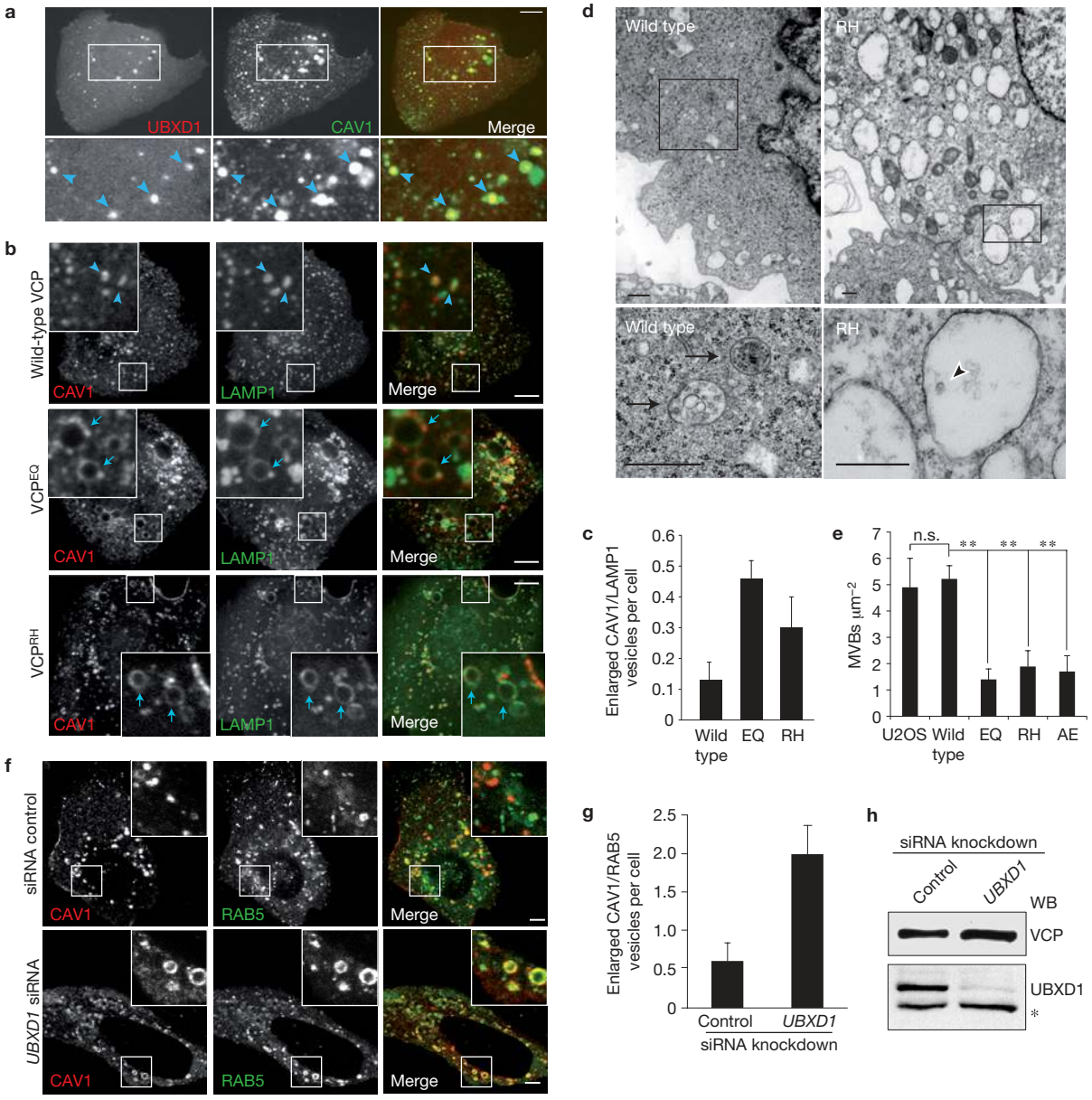

Figure 3 Overexpression of VCP mutants or depletion of UBXD1 affect CAV1 transport to endolysosomes. (**a**) CAV1 and UBXD1 co-localize on early and late endosomes. UBXD1–mCherry and CAV1–GFP were transiently expressed and visualized in live U2OS cells by spinning-disc confocal microscopy. Arrowheads indicate compartments showing co-localization. Manders' co-localization coefficient was 0.955, compared with 0.079 for mCherry alone (not shown), $n = 16$ cells per condition. See Supplementary Fig. S2a for co-localization with endosome markers. Scale bar, 10 µm. The insets in **a**,**b** and **f** show magnifications of the areas outlined in the main panels. (**b**) Expression of wild-type VCP, VCP^{EQ} or VCP^{RH} variants was induced by doxycycline for 24 h in stable U2OS cells transiently expressing CAV1–RFP and LAMP1–GFP. Live cells were visualized by spinning-disc confocal microscopy. The arrowheads indicate CAV1 localizing to late endosome/lysosomes. The arrows indicate CAV1 on enlarged late endosomes. Scale bars, 10 µm. (**c**) The number of enlarged LAMP1-positive vesicles (>0.8 µm diameter) with CAV1 at the limiting membrane (error bars represent s.d., three independent experiments, >140 cells per condition). (**d**) Electron micrographs of stable U2OS cells expressing wild-type VCP or VCP^{RH}. Arrows indicate MVBs. The arrowhead indicates a single intraluminal vesicle. The bottom images are magnifications of the areas outlined in the top images. Scale bars, 500 nm. (**e**) Quantification, number of MVBs per square micrometre of cytoplasm. Error bars represent s.d., $n = 10$ cells per condition. **, $P < 0.05$. (**f**) Cellular depletion of UBXD1 affects endosomal sorting of CAV1. U2OS cells were transfected with control or *UBXD1* siRNA oligonucleotides. CAV1–RFP and RAB5–GFP were visualized in live cells by confocal microscopy. Scale bars, 5 µm. (**g**) Number of enlarged CAV1/RAB5-positive vesicles (>1 µm diameter; error bars represent s.d., four independent experiments, >130 cells per condition). (**h**) After imaging, cells were lysed and depletion efficiency was confirmed by western blot (WB) analysis. The asterisk marks the position of a non-specific band. Uncropped images of blots are shown in Supplementary Fig. S6.

known as PTRF, polymerase I and transcript release factor), but not of other plasma membrane proteins dysferlin, dystrophin and dystrophin-associated glycoproteins (Supplementary Fig. S4b,c). These data provide evidence that disease-associated mutations of VCP specifically interfere with caveolin trafficking in cultured cells and patient tissue.

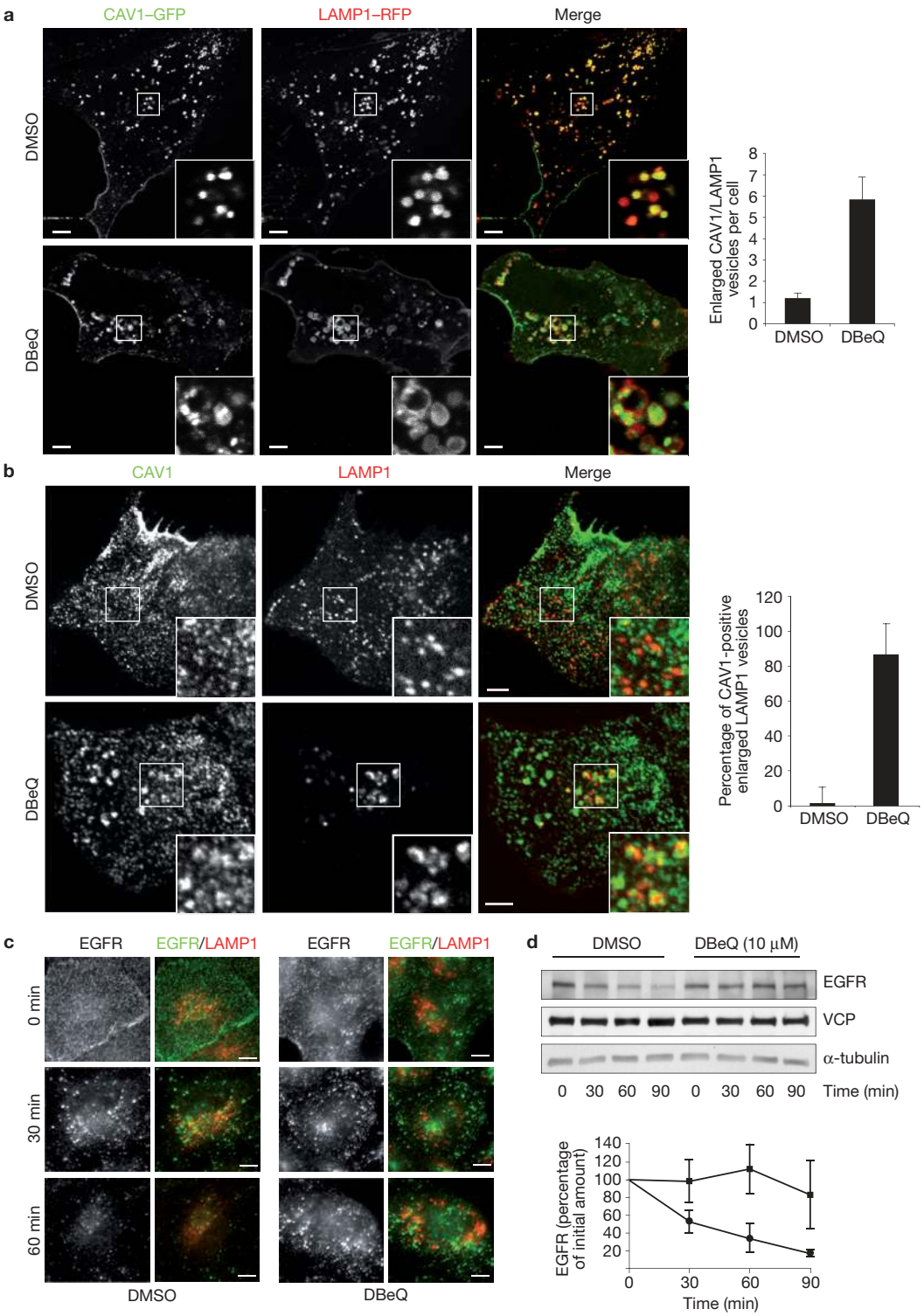

Figure 4 Chemical inhibition of VCP with DBeQ impairs CAV1 trafficking and delays degradation of the EGFR. (**a**) Left, laser scanning confocal sections of live U2OS cells transiently expressing CAV1–GFP and LAMP1–RFP after treatment with 10 μM DBeQ or solvent alone (dimethylsulphoxide, DMSO) for 6 h. The insets in the micrographs in **a** and **b** show magnifications of the areas outlined in the main panels. Scale bars, 5 μm. Right, the number of enlarged LAMP1-positive vesicles with CAV1 at the limiting membrane (error bars represent s.d., three independent experiments, >100 cells per condition). (**b**) Left, spinning-disc confocal sections of endogenous CAV1 and LAMP1 immunolocalization after treatment as in **a**. Scale bars, 3 μm. Right, quantification of the fraction of enlarged LAMP1-positive vesicles (>0.5 μm diameter) with CAV1 accumulation (error bars represent s.d., $n = 30$ cells per condition). (**c**) EGFR and LAMP1 were immunolocalized in CV-1 cells at the indicated times after EGF stimulation. DBeQ treatment, 10 μM for 5 h. Scale bars, 10 μm. (**d**) Top, western blot analysis of the EGFR in HEK293 cells at indicated times after EGF stimulation with or without DBeQ treatment as in **a**. Bottom, quantification of electrochemiluminescence signals on film. error bars represent s.d., $n = 5$. Uncropped images of blots are shown in Supplementary Fig. S6.

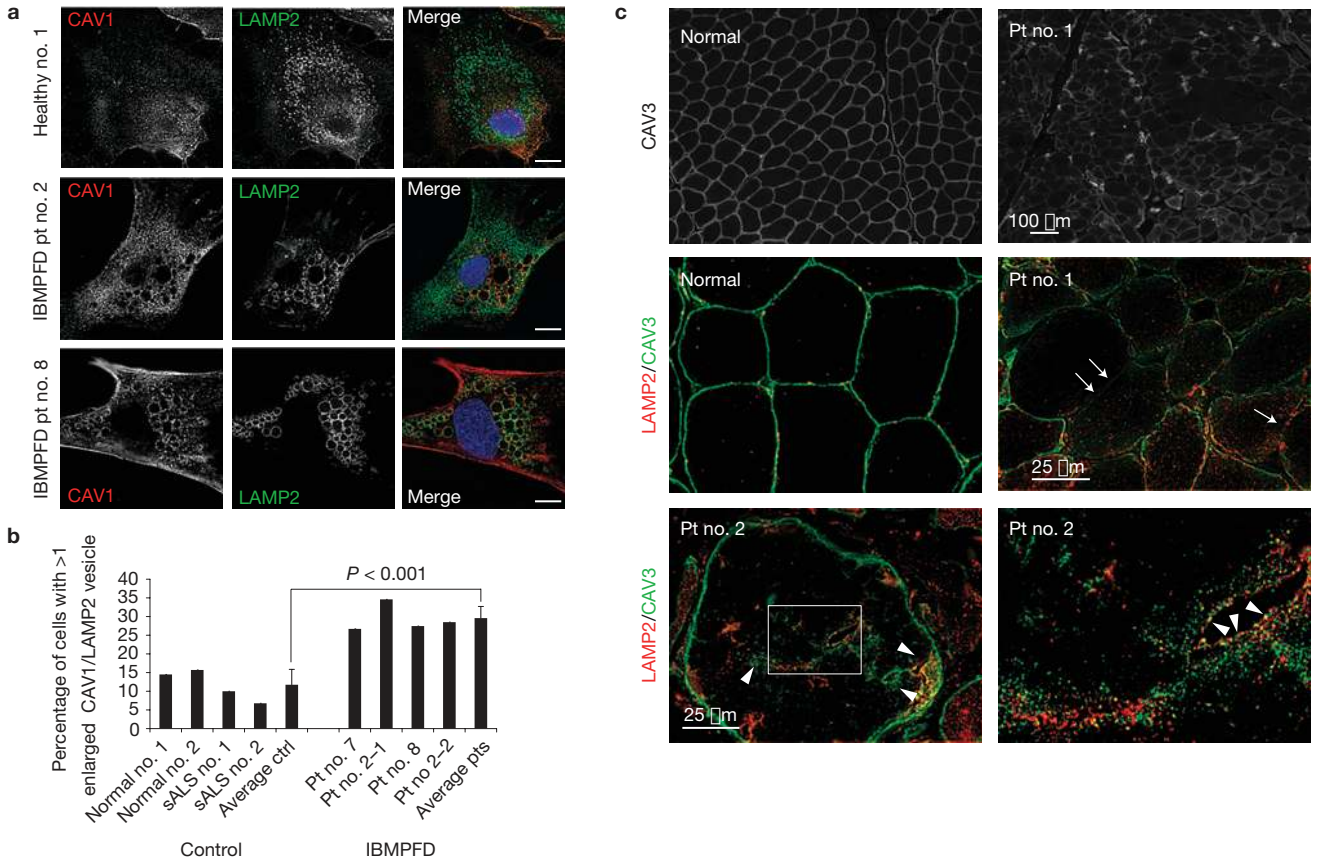

Figure 5 Mislocalization of caveolin in fibroblasts and muscle tissue of IBMPFD patients. (**a**) Cultured skin fibroblasts from two healthy donors, two patients with sALS and three IBMPFD patients were fixed, immunostained with antibodies to CAV1 and LAMP2 and imaged by epifluorescence microscopy. Only cells of one healthy control, and of IBMPFD patients no. 2 (pt no. 2, harbouring the VCP^{R155H} mutation) and no. 8 (L198W mutation) are shown. See Supplementary Table S2 for patient demographics. Scale bars, 10 μm. (**b**) Percentage of cells in **a** with more then one CAV1/LAMP2-positive vesicle. Average and s.d. (error bars) are from four control, and four IBMPFD cell isolates (two of pt no. 2, denoted 2-1 and 2-2, one of no. 7 and no. 8 each), respectively, with >100 cells each. Significance (*t*-test) is indicated. (**c**) Muscle tissue sections of a healthy individual and IBMPFD patients. Immunohistochemistry as indicated. Note the accumulation of CAV3 with LAMP2 in the sarcoplasm (arrowheads) and specific delocalization of CAV3 from the sarcolemma (arrows). The bottom right image shows a magnification of the area outlined in the bottom left image. See Supplementary Fig. S4 for localization of unaffected control sacrolemmal proteins and additional patient samples.

VCP has well-established roles in facilitating proteasome-dependent degradation of polyubiquitylated proteins. Our results now link VCP and UBXD1 to ubiquitin-dependent membrane sorting at endosomes and degradation in lysosomes, and imply that this pathway is impaired in IBMPFD. VCP binds to a mono-ubiquitylated cargo substrate, CAV1, on endosomes and is critical for its transport to endolysosomes. Blocking VCP binding of CAV1 (with IBMPFD-associated mutations) or its protein segregase activity (with the EQ mutation or the DBeQ inhibitor) leads to accumulation of CAV1 at the limiting membrane of late endosomes. Given that VCP targets SDS-resistant CAV1 oligomers (Fig. 2), one possible scenario is that VCP helps to segregate stable, SDS-resistant CAV1 assemblies to facilitate their transport to the lumen of endolysosomes. Cellular depletion of the UBXD1 cofactor also affected CAV1 trafficking (Fig. 3f,g), but not the VCP–CAV1 interaction (data not shown), indicating that UBXD1 may help VCP in substrate-processing rather than acting as a substrate adapter. Interestingly, another cofactor, phospholipase A2-activating protein (PLAA; also known as UFD3) that we identified in our screen (Fig. 1a) was shown to function in sorting to late endosomes in yeast[34], implying a conserved role of VCP in this process. Chemical inhibition of VCP also affected EGFR sorting, indicating that VCP is more generally involved in trafficking of endocytic cargo. Our results do not exclude that compromised interaction with other cofactors reported during the course of this study may be relevant[15]. At least in the case of the E4B (also known as UFD2) cofactor however, the decrease in the level of binding seems minor when compared with CAV1 and UBXD1 in our laboratory (Supplementary Fig. S5). Taken together, we propose that impaired endosomal trafficking constitutes an important aspect in the cytopathology caused by IBMPFD-associated mutations.

Consistently, we show that VCP mutations are associated with CAV3 mislocalization in IBMPFD patient muscle, identical to that observed in transgenic mice expressing VCP^{RH} (ref. 35). Importantly, myopathy-causing mutations in CAV3 result in a similar mislocalization[36]. These include a P104L missense mutation in CAV3, whose equivalent P132L in CAV1 abolishes VCP binding (Fig. 2e). This supports the notion that CAV3 mislocalization in IBMPFD patient tissue may contribute to inclusion body myopathy pathogenesis. Impaired CAV1 and receptor sorting may also be relevant to Paget's disease of bone, which is commonly caused by defective ubiquitin-dependent signal transduction from the plasma membrane in osteoclasts[37]. Moreover,

the third phenotypic feature in IBMPFD is fronto-temporal dementia. Of note, one pathologically similar form of fronto-temporal dementia is associated with mutations in CHMP2B, another factor that is essential for endosomal sorting and MVB biogenesis[38]. In analogy, impaired VCP-mediated endosomal sorting may therefore even be relevant for the pathogenesis in neurons. □

METHODS

Methods and any associated references are available in the online version of the paper at http://www.nature.com/naturecellbiology

Note: Supplementary Information is available on the Nature Cell Biology website

ACKNOWLEDGEMENTS

We thank A. Helenius, M. Kaiser, P. Hanson and A. Pestronk for discussions and reagents, G. Dey for image analysis software, C. Brasseur and G. Csucs for technical help, and R. Deshaies for sharing results before publication. This work was supported by grants from the ETH (26/05-2 and 25/08-1), the DFG priority programme SPP1365/2 and the Fondation Suisse de recherche sur les maladies musculaires (to H.M.). C.C.W. is supported by the NIH (R01 AG031867) and the Muscular Dystrophy Association.

AUTHOR CONTRIBUTIONS

D.R. generated cells, isolated VCP complexes and carried out the biochemical analyses with help from P.K., S.S. and S.B., and M.V. and M.B. carried out microscopy. A.H. helped design experiments and carried out the co-localization analysis. H.L, T.G., M.G. and R.A. carried out mass spectrometry analysis. C.L., R.H.B. and C.C.W. carried out electron microscopy and analysis of patient material. H.M. conceived the project and wrote the manuscript.

COMPETING FINANCIAL INTERESTS

The authors declare no competing financial interests.

Published online at http://www.nature.com/naturecellbiology
Reprints and permissions information is available online at http://www.nature.com/reprints

1. Jentsch, S. & Rumpf, S. Cdc48 (p97): A 'molecular gearbox' in the ubiquitin pathway? *Trends Biochem. Sci.* **32,** 6–11 (2007).
2. Meyer, H. & Popp, O. Role(s) of Cdc48/p97 in mitosis. *Biochem. Soc. Trans.* **36,** 126–130 (2008).
3. Ye, Y. Diverse functions with a common regulator: ubiquitin takes command of an AAA ATPase. *J. Struct. Biol.* **156,** 29–40 (2006).
4. Watts, G. D. *et al.* Inclusion body myopathy associated with Paget disease of bone and frontotemporal dementia is caused by mutant valosin-containing protein. *Nat. Genet.* **36,** 377–381 (2004).
5. Weihl, C. C., Pestronk, A. & Kimonis, V. E. Valosin-containing protein disease: inclusion body myopathy with Paget's disease of the bone and fronto-temporal dementia. *Neuromuscul. Disord.* **19,** 308–315 (2009).
6. Hayer, A. *et al.* Caveolin-1 is ubiquitinated and targeted to intraluminal vesicles in endolysosomes for degradation. *J. Cell Biol.* **191,** 615–629 (2010).
7. Jarosch, E., Geiss-Friedlander, R., Meusser, B., Walter, J. & Sommer, T. Protein dislocation from the endoplasmic reticulum–pulling out the suspect. *Traffic* **3,** 530–536 (2002).
8. Meyer, H. H., Shorter, J. G., Seemann, J., Pappin, D. & Warren, G. A complex of mammalian Ufd1 and Npl4 links the AAA-ATPase, p97, to ubiquitin and nuclear transport pathways. *EMBO J.* **19,** 2181–2192 (2000).
9. Schuberth, C. & Buchberger, A. UBX domain proteins: major regulators of the AAA ATPase Cdc48/p97. *Cell Mol. Life Sci.* **65,** 2360–2371 (2008).
10. Alexandru, G. *et al.* UBXD7 binds multiple ubiquitin ligases and implicates p97 in HIF1α turnover. *Cell* **134,** 804–816 (2008).
11. Tresse, E. *et al.* VCP/p97 is essential for maturation of ubiquitin-containing autophagosomes and this function is impaired by mutations that cause IBMPFD. *Autophagy* **6,** 217–227 (2010).
12. Ju, J. S. *et al.* Valosin-containing protein (VCP) is required for autophagy and is disrupted in VCP disease. *J. Cell Biol.* **187,** 875–888 (2009).
13. Janiesch, P. C. *et al.* The ubiquitin-selective chaperone CDC-48/p97 links myosin assembly to human myopathy. *Nat. Cell Biol.* **9,** 379–390 (2007).
14. Ju, J. S., Miller, S. E., Hanson, P. I. & Weihl, C. C. Impaired protein aggregate handling and clearance underlie the pathogenesis of p97/VCP associated disease. *J. Biol. Chem.* **283,** 30289–30299 (2008).
15. Fernandez-Saiz, V. & Buchberger, A. Imbalances in p97 co-factor interactions in human proteinopathy. *EMBO Rep.* **11,** 479–485 (2010).
16. Weihl, C. C., Dalal, S., Pestronk, A. & Hanson, P. I. Inclusion body myopathy-associated mutations in p97/VCP impair endoplasmic reticulum-associated degradation. *Hum. Mol. Genet.* **15,** 189–199 (2006).
17. Ye, Y., Meyer, H. H. & Rapoport, T. A. Function of the p97-Ufd1-Npl4 complex in retrotranslocation from the ER to the cytosol: dual recognition of nonubiquitinated polypeptide segments and polyubiquitin chains. *J. Cell Biol.* **162,** 71–84 (2003).
18. Ramadan, K. *et al.* Cdc48/p97 promotes reformation of the nucleus by extracting the kinase Aurora B from chromatin. *Nature* **450,** 1258–1262 (2007).
19. Keller, A., Eng, J., Zhang, N., Li, X. J. & Aebersold, R. A uniform proteomics MS/MS analysis platform utilizing open XML file formats. *Mol. Syst. Biol.* **1,** 0017 (2005).
20. Iwawaki, T., Akai, R., Kohno, K. & Miura, M. A transgenic mouse model for monitoring endoplasmic reticulum stress. *Nat. Med.* **10,** 98–102 (2004).
21. Madsen, L. *et al.* Ubxd1 is a novel co-factor of the human p97 ATPase. *Int. J. Biochem. Cell Biol.* **40,** 2927–2942 (2008).
22. Parton, R. G. & Simons, K. The multiple faces of caveolae. *Nat. Rev. Mol. Cell Biol.* **8,** 185–194 (2007).
23. Hayer, A., Stoeber, M., Bissig, C. & Helenius, A. Biogenesis of caveolae: stepwise assembly of large caveolin and cavin complexes. *Traffic* **11,** 361–382 (2010).
24. Scheiffele, P. *et al.* Caveolin-1 and -2 in the exocytic pathway of MDCK cells. *J. Cell Biol.* **140,** 795–806 (1998).
25. Monier, S. *et al.* VIP21-caveolin, a membrane protein constituent of the caveolar coat, oligomerizes *in vivo* and *in vitro*. *Mol. Biol. Cell* **6,** 911–927 (1995).
26. Tagawa, A. *et al.* Assembly and trafficking of caveolar domains in the cell: caveolae as stable, cargo-triggered, vesicular transporters. *J. Cell Biol.* **170,** 769–779 (2005).
27. Mundy, D. I., Machleidt, T., Ying, Y. S., Anderson, R. G. & Bloom, G. S. Dual control of caveolar membrane traffic by microtubules and the actin cytoskeleton. *J. Cell Sci.* **115,** 4327–4339 (2002).
28. Haglund, K., Di Fiore, P. P. & Dikic, I. Distinct monoubiquitin signals in receptor endocytosis. *Trends Biochem. Sci.* **28,** 598–603 (2003).
29. Sargiacomo, M. *et al.* Oligomeric structure of caveolin: implications for caveolae membrane organization. *Proc. Natl Acad. Sci. USA* **92,** 9407–9411 (1995).
30. Pol, A. *et al.* Cholesterol and fatty acids regulate dynamic caveolin trafficking through the Golgi complex and between the cell surface and lipid bodies. *Mol. Biol. Cell* **16,** 2091–2105 (2005).
31. Rape, M. *et al.* Mobilization of processed, membrane-tethered SPT23 transcription factor by CDC48(UFD1/NPL4), a ubiquitin-selective chaperone. *Cell* **107,** 667–677 (2001).
32. Lee, H. *et al.* Caveolin-1 mutations (P132L and null) and the pathogenesis of breast cancer: caveolin-1 (P132L) behaves in a dominant-negative manner and caveolin-1 (−/−) null mice show mammary epithelial cell hyperplasia. *Am. J. Pathol.* **161,** 1357–1369 (2002).
33. Chou, T. F. *et al.* Reversible inhibitor of p97, DBeQ, impairs both ubiquitin-dependent and autophagic protein clearance pathways. *Proc. Natl Acad. Sci. USA* **108,** 4834–4839 (2011).
34. Ren, J., Pashkova, N., Winistorfer, S. & Piper, R. C. DOA1/UFD3 plays a role in sorting ubiquitinated membrane proteins into multivesicular bodies. *J. Biol. Chem.* **283,** 21599–21611 (2008).
35. Weihl, C. C., Miller, S. E., Hanson, P. I. & Pestronk, A. Transgenic expression of inclusion body myopathy associated mutant p97/VCP causes weakness and ubiquitinated protein inclusions in mice. *Hum. Mol. Genet.* **16,** 919–928 (2007).
36. Minetti, C. *et al.* Mutations in the caveolin-3 gene cause autosomal dominant limb-girdle muscular dystrophy. *Nat. Genet.* **18,** 365–368 (1998).
37. Goode, A. & Layfield, R. Recent advances in understanding the molecular basis of Paget disease of bone. *J. Clin. Pathol.* **63,** 199–203 (2010).
38. Skibinski, G. *et al.* Mutations in the endosomal ESCRTIII-complex subunit CHMP2B in frontotemporal dementia. *Nat. Genet.* **37,** 806–808 (2005).

DOI: 10.1038/ncb2301

METHODS

Plasmid constructs. The coding sequence of rat VCP was PCR-cloned with a carboxy-terminal Myc/Strep-tag (amino acid sequence: EQKLISEEDL-NMHTG-WSHPQFEK) into the KpnI/BamHI sites of pcDNA5FRT/TO (Invitrogen). Missense mutations were introduced according to the Quikchange protocol and the total sequence was confirmed. Human UBXD1 was cloned with a C-terminal 3×haemagglutinin (HA)-tag or mCherry into pIRESpuro2 (Invitrogen). Constructs for CAV1–HA, CAV1–Myc, CAV1$^{K^*R}$–Myc, CAV1–monomeric enhanced GFP and CAV1–RFP were described previously[6,23]. LAMP1–GFP/–RFP, LC3–GFP and HA–ubiquitin were gifts from J. Gruenberg (University of Geneva, Switzerland), T. Yoshimori (National Institute of Genetics, Osaka, Japan) and P. DeCamilli (Yale University, USA), respectively.

Cell culture and transfections. Stable inducible HEK293 cells expressing Myc/Strep-tagged VCP variants were generated with the Flp-In T-REx system (Invitrogen) according to the manufacturer's protocol and single clones were selected. Stable inducible U2OS cell lines expressing VCP variants were described previously[14]. Cells were maintained in DMEM supplemented with 10% FCS in the presence of penicillin/streptomycin, and stable cell lines were additionally supplemented with 50 μg ml^{-1} hygromycin and 100 μg ml^{-1} zeocin (for U2OS) or 100 μg ml^{-1} hygromycine and 15 μg ml^{-1} blasticidine (for HEK293). Expression was induced by 1 μg ml^{-1} doxycycline. HEK293 cells were transfected using calcium phosphate, CV-1 using electroporation (AMAXA) and U2OS using JetPei or JetPrime reagent (Polyplus). For siRNA experiments, U2OS cells were transfected with *UBXD1*-targeting (CCAGGUGAGAAAGGAACUUTT) or non-targeting control (UUCUCCGAACGUGUCACGUTT) oligomers at 15 nM final concentration with Lipofectamine 2000 (Invitrogen) according to the manufacturer's instructions and cells were analysed after 48 h.

Patient fibroblasts and skeletal muscle. Patient dermal fibroblasts and muscle were obtained under an approved IRB protocol at Washington University School of Medicine. All experiments were carried out with fibroblasts at a matched passage number of less than 10. One fibroblast line (GM20926) was obtained from Coriell Cell repositories. Fibroblasts were grown for 1–2 days, methanol-fixed and processed for immunodetection. For cell counting, >100 fibroblasts were counted from >10 randomly identified fields with a ×40 objective using two sets of coverslips/fibroblast culture. CAV1 immunoreactive vacuoles were identified as a full circle with an empty lumen. For statistics, each control or IBMPFD fibroblast line was treated as an independent experiment (therefore an $N = 4$, and the average and s.e.m. from these four control cell lines was calculated). Frozen tissue was sectioned (10 μM), acetone-fixed and processed for immunodetection. For some antibodies, a biotinylated secondary antibody was used and then detected using a Vectastain ABC kit (Vector Labs). Specimens were examined using a fluorescence microscope (Nikon 80i upright) and a Roper Scientific EZ monochrome CCD (charge-coupled device) camera with deconvolution software analysis (NIS Elements, Nikon) at room temperature.

Electron microscopy. For thin-section electron microscopy, cells were grown to 70% confluence in a 100 mm dish and induced to express VCP variants for 16 h. For sample preparation, trypsinized cells were collected, washed in phosphate-buffered saline (PBS), fixed in 2.5% glutaraldehyde in sodium cacodylate, embedded, sectioned and stained with uranyl acetate according to standard procedures. For quantification, 10 randomly generated 300 × 300 μm images were taken for each condition. An MVB was identified as a vacuole with a diameter of >200 nm containing three or more internal vesicles.

Statistical analysis. Statistical analyses were carried out with the unpaired two-sided t-test. $P < 0.05$ (**) was considered statistically significant.

Fluorescence imaging and co-localization analysis. For live-cell imaging, U2OS cells were seeded into μ-Slide 8-well chambers (Ibidi) one day before transfection or induction. Live-cell imaging was carried out using a Zeiss Axiovert 200 M microscope equipped with a Yokogawa CSU10 spinning-disc confocal unit and a temperature/CO_2-controlled incubator. Images were acquired using a Hamamatsu C9100-13 EMCCD camera, an argon–krypton laser (Spectra Physics) and a ×100/1.4 NA PlanApo oil-immersion objective. Acquisition was driven by Metamorph (Molecular Devices). Alternatively, a Leica TCS SP5 laser scanning microscope, with a ×100/1.49 NA oil-immersion objective was used. For quantification of UBXD1–mCherry co-localization with CAV1–GFP or CAV1–HA, the JACoP plugin in ImageJ software[39] was used and the Manders' coefficient was calculated for signal overlap: the fraction of the UBXD1–mCherry signal overlapping with CAV1–GFP (Fig. 3a) or the fraction of the CAV1–HA immuno-signal overlapping with UBXD1–mCherry (Supplementary Fig. S2d). For quantification with endosomal markers, live cells were imaged using a Zeiss epifluorescence microscope equipped with a Hamamatsu camera, a 100 W HBO lamp and Metamorph software. Automated co-localization analysis was carried out using a Matlab routine to detect endosomal structures on epifluorescence images of live cells acquired with an Olympus IX71 system and to determine the overlap between D1–mCherry and endosomal markers as described previously[6]. Detected UBXD1–mCherry structures overlapping at least 40% with endosomal markers were considered co-localizing. For indirect immunofluorescence microscopy, cells were seeded on coverslips and fixed in 4% formaldehyde. Epifluorescence images were taken on a Nikon Eclipse Ti microscope with an Andor DR-328G-C01-SIL camera. For confocal images, a Yokogawa CSU-X1 unit attached to the same microscope was used and images were acquired with an Andor iXon X3 EMCCD camera.

Flow cytometry. Stable HEK293 cells were transfected with the pCAX-F–XBP1$^{\Delta DBD}$–Venus construct[20] and VCP variants were induced by doxycycline treatment. After 24 h, cells were fixed and XBP1–Venus intensities were measured at 488 nm in a FACSCalibur (BD Biosciences) flow cytometer.

Antibodies and other reagents. Anti-p97, anti-p47, anti-NPL4 and anti-UFD1 5E2 (Abcam) were used as described previously[18]. Anti-UBXD1 (1:1,000, E43) was raised in rabbits against full-length human UBXD1 fused to glutathione *S*-transferase (GST). For western blotting after immunoprecipitation, biotinylated anti-p47 and anti-UBXD1 were detected with steptavidin–HRP. Anti-Myc 9E10 (1:1,000), anti-CAV1 N20 (1:500, Santa Cruz, sc-894), anti-HA HA11 (1:2,000, Covance), anti-UFD2/E4 (1:1,000, BD Biosciences), anti-Ub FK2 (1:500, Millipore), anti-LAMP1 (1:500, H4A3) and anti-LAMP2 (1:1,000, Santa Cruz), rabbit anti-PTRF/cavin-1 (1:500, Bethyl Labs), rabbit anti-CAV3 (1:1,500, Affinity Bioreagents), mouse anti-dysferlin (1:250, Vector Labs), anti-γ-sarcoglycan (1:500, Novocastra) and mouse anti-dystrophin (1:500, Novocastra) were purchased. AlexaFluor-conjugated secondary antibodies for immunofluorescence microscopy (1:600) and lysotracker green were purchased from Invitrogen. Lysotracker was incubated at 100 nM for 1 h. DBeQ was purchased (Interbioscreen).

Immuno- and affinity-isolation. For protein isolation, cells were lysed in extraction buffer (150 mM KCl, 5 mM $MgCl_2$, 25 mM Tris-HCl, 1% Triton X-100, 5% glycerol, 2 mM β-mercaptoethanol, at pH 7.4, and Roche Complete EDTA-free protease inhibitors) for 20 min on ice and cleared for 15 min at 16,000*g*. Immunoprecipitations and pulldown experiments were done in extraction buffer supplemented with 1 mg ml^{-1} BSA using Strep-Tactin Sepharose (IBA Biotagnology), anti-c-Myc agarose (Sigma), anti-HA agarose (Sigma) or specific antibodies and Protein-G–Sepharose (GE Healthcare). For sequential isolation, VCP complexes were isolated with Strep-Tactin and eluted at 95 °C in 1% SDS. Samples were diluted with extraction buffer to 0.1% SDS and CAV1 was immunoprecipitated using anti-CAV1 (N20).

EGFR degradation assay. Cells were serum-starved in DMEM for 16 h and treated with 10 μM DBeQ or solvent alone for a total of 6 h. EGFR internalization was induced by the addition of 50 ng ml^{-1} EGF (Immunotools) for indicated times before lysis in extraction buffer or fixation. Western blot results were quantified from scans with Bio-1D software (Vilber Lourmat). Microscopy was carried out as stated above.

Analysis of SDS-resistant CAV1 oligomers and sucrose velocity gradients. CV-1 cells were transfected with VCP variants and lysed after 24 h in extraction buffer. Cleared lysates (212 μg protein) were diluted to 200 μl. VCP was isolated with Strep-Tactin Sepharose and eluted in 10 mM biotin in extraction buffer. Western blot analysis was done as described previously[24]. Briefly, 5× low-SDS sample buffer (50 mM Tris-HCl at pH 6.8, 0.5% SDS, 1.9% glycerol, 0.5 M dithiothreitol and 0.2% bromphenol blue) was added to eluates, and samples were analysed on a gradient gel without boiling (NuPAGE Novex 4–12% Bis-Tris Gel, Sigma) usingNuPAGE MOPS SDS running buffer. Proteins were semi-dry blotted onto polyvinylidene fluoride membrane and processed for immunodetection. Velocity gradients were run as described previously[23] with lysates from stable HEK293 cells induced for 24 h. Western blots were quantified using a GS-800 calibrated densitometer (Biorad) and ImageJ software (http://rsb.info.nih.gov/ij/).

VCP tandem isolation for mass spectrometry analysis. Cleared lysates (~20 mg protein) were diluted to 5 ml with extraction buffer supplemented with 1 mg ml^{-1} BSA and 1 μM avidin (IBA Biotechnology). Samples were incubated with 400 μl Strep-Tactin Sepharose slurry. Bound proteins were eluted with 2.5 mM biotin and incubated with 200 μl anti-c-Myc–agarose slurry (Sigma). Proteins were eluted in 0.2 M glycine at pH 2.5 and the pH was adjusted to 8.8 with ammonium bicarbonate. For reduction, proteins were incubated in 5 mM TCEP (*tris* (2-carboxyethyl)phosphine) for 1 h at 37 °C, followed by incubation with 25 mM iodoacetamide. Proteins were trypsin digested and peptides were purified on C18 MicroSpin columns (Harvard Apparatus) in 5% acetonitrile and 0.1% trifluoroacetic acid, dried and resuspended in 0.1% formic acid.

LC–MS/MS analysis. LC–MS/MS analysis was carried out using an Agilent 1100 series pump (Agilent Technologies) and an LTQ mass spectrometer (Thermo Electron). The set-up of the microcolumn reversed-phase liquid chromatography system and the capillary column were described previously[40]. The electrospray voltage was set to 1.8 kV. Mobile phase A was 0.1% formic acid and mobile phase B was 100% acetonitrile (Sigma). For analysis, a separating gradient from 5% to 45% mobile phase B over 40 min at 0.3 μl min^{-1} was applied. The three most abundant precursor ions in each mass spectrometry scan were selected for collision-induced dissociation if the intensity of the precursor ion exceeded 10,000 ion counts. The dynamic exclusion window was set to 2 min.

MS2 peptide assignments and MS1 alignment. Acquired MS2 scans were searched against the human International Protein Index protein database (version 3.26) using the XTandem search algorithm with the *k*-score plugin[40]. *In silico* trypsin digestion was carried out C-terminally of lysine and arginine (unless followed by proline) in fully tryptic peptides. The allowed mono-isotopic mass error for the precursor ions was 2 Da. A fixed residue modification parameter was set for carboxyamidomethylation (+57 Da) of cysteine residues. Oxidation of methionine (+16 Da) was set as a variable residue modification parameter. Model refinement parameters were set to allow phosphorylation (+80 Da) of serine, threonine and tyrosine residues as variable modifications. Search results were evaluated on the Trans Proteomic Pipeline (TPP version 3.2) using PeptideProphet and ProteinProphet[19]. Background proteins identified in isolates from uninduced cells were subtracted.

39. Bolte, S. & Cordelieres, F. P. A guided tour into subcellular colocalization analysis in light microscopy. *J. Microsc.* **224,** 213–232 (2006).
40. MacLean, B., Eng, J. K., Beavis, R. C. & McIntosh, M. General framework for developing and evaluating database scoring algorithms using the TANDEM search engine. *Bioinformatics* **22,** 2830–2832 (2006).